Constrained Maximum Power Extraction in PMVG Wind Turbine System With Predictive Rotor Position Bias-Based Current Angle Control for Power Factor Improvement

Ganesh Mayilsamy, Byoung Chang Jeong, Seong Ryong Lee, Jae Hoon Jeong, and Young Hoon Joo

***Abstract*—This study aims to present a power factor improvement constrained maximum power extraction for the permanent magnet vernier generator (PMVG)-based wind turbine system (WTS). The PMVG power factor suffers due to design considerations and can be improved by the current angle control (CAC). To do this, a finite angle-rotor position bias (FA-RPB) scheme is proposed by utilizing the principle of model predictive control. The FA-RPB-based CAC scheme is formulated to identify the optimum rotor position bias through cost function optimization and ensures the maximum power factor operation in PMVG. At this time, the electromagnetic torque developed by the generator is modified accordingly due to the introduction of RPB. Consequently, the maximum power extraction of WTS based on the optimum torque control is affected. Therefore, this study aims to enhance the PMVG stator power factor by adapting an RPB-constrained maximum power extraction strategy under CAC through constrained current reference to the control system. Finally, a 5-kW laboratory prototype verifies the enhanced operation of PMVG-based WTSs and the comparative results are summarized.**

***Index Terms*—Current angle control (CAC), permanent magnet vernier generator (PMVG), power factor improvement, wind turbine system (WTS).**

I. Introduction

THE high-torque density permanent magnet (PM) generators are recently gaining attention in direct drive (DD) wind turbine systems (WTSs). Such machines are expected to be an effective alternative to the PM synchronous generators (PMSGs) in the low-speed high-power DD WTS applications [1], [2]. In this trend, the transverse flux PM machines, flux switching machines, flux reversal machines, and permanent magnet vernier generators (PMVGs) are a few recently introduced novel machines [3]. The flux modulation property and the magnetic gearing effect in such machines integrate the low-speed operation with a higher shaft torque. In addition, reduced torque ripples in PMVG relatively reduce the noise, shaft vibration, and enhance the WTS structural integrity [4].

The PMVG's magnetically coupled structure and the additional PM modulation flux provide increased power density and achieves relatively higher torque density with minimum ripples [5]. It is a much desirable quality for a WTS application, which is usually operating with minimum rotor speed. Moreover, the maximum torque per ampere trajectory identification with physics-informed network, improved conformal mapping and other advanced analytical machine design procedures make it easier to design flux modulated machines for any specific applications with improved torque density [6], [7]. Therefore, the PMVG is emerging as an attractive candidate for DD WTS applications [8], [9].

Despite the features such as better performance regarding low-speed operation with higher shaft torque, the PMVGs are highly susceptible to lower power factor (PF) [10]. In Kim's [3] work, it is indicated that, the PMVG PF in the WTS application goes less than 0.6 under rated operating conditions. This is due to the higher slot per pole per phase number, and high electrical frequency. In addition, the magnetic gearing effect in PMVG has an indirect relationship with the PF. The above-mentioned phenomenon critically influences the volt–ampere (VA) rating and leads to a higher VA rating as compared to a PMSG. As a consequence, the machine-side converter (MSC) has to handle increased reactive power flow and required to be designed with a higher VA rating, which leads to increased hardware cost and complexity in converter design [11]. In addition, the increased reactive power leads to reduction in converter active power transfer capacity resulting to lower energy production, stability concerns, harmonic distortion, and system protection challenges [12]. Therefore, PF improvement is inevitable in PMVG WTS applications to reduce the counter effects of reactive power such as converter switching losses, thermal stress and voltage instability [13].

Manuscript received 16 October 2023; revised 7 January 2024 and 29 February 2024; accepted 11 April 2024. Date of publication 18 April 2024; date of current version 16 May 2024. This work was supported in part by Basic Science Research Program under Grant NRF-2016 R1A6A1A03013567 and Grant NRF-2021R1A2B5B01001484 and in part by the framework of International Cooperation Program under Grant NRF-2022 K2A9A2A06045121 through the National Research Foundation of Korea (NRF) funded by the Ministry of Education. Recommended for publication by Associate Editor F. D. Freijedo. *(Corresponding author: Young Hoon Joo.)*

Ganesh Mayilsamy, Seong Ryong Lee, Jae Hoon Jeong, and Young Hoon Joo are with the Research Center for Wind Energy Systems, Kunsan National University, Gunsan 573 -701, Republic of Korea (e-mail: yhjoo@kunsan.ac.kr).

Byoung Chang Jeong is with R&D center, Realtech Company Ltd., Yongin 17043, Republic of Korea.

Color versions of one or more figures in this article are available at https://doi.org/10.1109/TPEL.2024.3389998.

Digital Object Identifier 10.1109/TPEL.2024.3389998

To deal with this, the surface PM vernier machines are researched on the basis of PM flux linkage and armature flux linkage for PF improvement [14]. In this sense, various topological modifications have been introduced with the idea of either increasing the PM flux linkage or reducing the armature flux linkage. Moreover, it focuses on the properties of various working flux densities in the machine with the inherent behavior of PMVG's phase current aligning to the induced emf. The topological modifications for PF improvement aim to alter the magnetic properties of the machine [15], [16]. Other than the topological modifications, the MSC vector control can contribute to PF improvement to a certain extent. It can be realized based on the principle of phase voltage orientation of current used in PMSG unity power factor (UPF) control [17].

Generally, the PMSG/PMVG vector control is formulated by calculating the stator-induced emf phase angle θ_e from the encoder-measured rotor position θ_m. Then, the θ_m, θ_e are bounded to the range $-\pi$ to π and employed in speed calculation, abc/dq and dq/abc transformations [18]. Therefore, the generator stator phase currents are usually oriented to the induced emf [19]. However, the UPF control for PMSG aims to achieve the phase currents to be oriented to the generator phase voltages. To do this, 1) either a suitable nonzero d-axis current (ZDC) is introduced to synchronize the phase current with the voltage, or 2) with zero d-axis current (ZDC), a required d-axis emf amplitude is intentionally created by modifying the θ_e to keep the d-axis stator voltage as zero [17], [20]. Since the PMSG's rated PF is in the range of 0.9–1, the modification in the current control (CC) angle to keep the d-axis stator voltage at zero will not greatly alter the other operating vectors. Accordingly, the PMSG UPF control is achieved by closed-loop current angle control (CAC) to the entire operating range [21], [22].

Besides, the high torque density PMVGs operate with a higher current rating and low PF than the PMSGs [23]. Therefore, compensating the d-axis stator voltage through the d-axis induced emf by adjusting the θ_e for PMVG UPF operation is limited to certain critical load. However, the PF can still be improved as compared to the conventional rotor position-oriented control. Accordingly, the optimum adjustment (denoted as θ_b^m) required to the encoder measured θ_m should be unique for each of the loads varying above the critical load. Any false adjustment to the θ_m beyond the critical load may either not be effective in PF improvement or lead to deteriorating the system control performance [24]. Therefore, the design of closed-loop CAC schemes employing the PF error or d-axis emf error is difficult. This is due to the load-dependent variation in the θ_e modification for PF improvement especially above the critical load [25].

On this account, model-based predictive controllers can be employed to identify the θ_e adjustment required to keep the minimum phase lag/lead angle between the stator voltage and current [26]. The finite control set-model predictive control (FCS-MPC) is known for its promising control nature for converters and motor drives with good dynamic performance, handling constraints/nonlinearities, and applying modulator-free switching states [27]. In which, the future behavior of an operating parameter is predicted for a finite number of control sets and an optimum state is applied based on cost function optimization [28], [29]. Besides, the predictive control schemes has been found to be an effective choice in multiphase PM machine control applications [30], [31] and converter switching applications with specific objectives [32]. Therefore, the optimum bias required to adjust the measured rotor position can be predicted through the finite angle-rotor position bias (FA-RPB) scheme underlying the FCS-MPC principle. The FA-RPB can predict the optimum bias from the discrete set of bias angles by cost function optimization with the objective of PF maximization. The finite set of bias angles can be decided based on the mathematical analysis employing the PMVG parameters similar to the rotor position estimation in Abdelrahem et al.'s [33] work.

The optimum bias is evaluated through FA-RPB with the constraint of keeping the PF unity until the critical load, and improving the PF from its typical value for above critical load operations. Moreover, the adjusted current angle through FA-RPB has a significant effect over the airgap flux and affects the electromagnetic torque developed in the armature [34]. As a result, the WTS rotor speed deviates from the optimum value and reaches to the new operating point, this will make the WTS to operate away from the optimum tip speed ratio (TSR). The maintenance of optimum TSR is crucial for WTS maximum power extraction (MPE) with traditional optimum torque control (OTC), which primarily depends on the mechanical parameter specification of the wind turbine [35]. Hence, to ensure the MPE of WTS, the effect of the FA-RPB modified current angle over the electromagnetic torque should be suitably compensated to maintain the optimum TSR. Therefore, a constrained maximum power extraction (CMPE) should be incorporated to the FA-RPB-based CAC in MSC vector control to ensure the optimum TSR.

In this context, to the best of our knowledge, these problems in PMVG-based WTSs have not been investigated in the previous literature. Therefore, this study aims to propose an FA-RPB for the CAC and CAC-CMPE operation of PMVG-based WTS. Contribution of this study is summarized as follows.

1) Steady state analysis is carried out under RPB-based CAC for PF improvement in PMVG. The effect of RPB (θ_b^m) over various operating vectors is analyzed.
2) An FA-RPB scheme is proposed to predict the optimum θ_b^m to improve the PMVG power factor by utilizing the principles of MPC.
3) An FA-RPB-CAC dependent CMPE is introduced to overcome the effect of θ_b^m over the generator torque.
4) Next, the effectiveness of the proposed CMPE is analyzed through experiments and comparative studies.
5) Finally, the applicability of presented scheme to the MW class PMVGs is substantiated through simulation results.

The rest of this article is organized as follows. Section II discusses the PMVG control preliminaries and power factor. Section III introduces the proposed FA-RPB to identify the optimum bias angle and PF improvement CMPE. Then, the method validation, quantitative analysis and comparison results are presented in Section IV. Finally, Section V concludes this article.

II. Preliminaries

A. Modeling of Wind Turbine and PMVG

The aerodynamic torque and one mass drive train model of WTS can be expressed as follows:

$$T_{\text{sh}} = 0.5\rho\pi R_b^5 \mathcal{C}_p \omega_m^2/\lambda^3 \tag{1}$$

$$\frac{d\omega_m}{dt} = \frac{1}{J_{\text{sh}}}(T_{\text{sh}} - T_e - f_v\omega_m) \tag{2}$$

where T_{sh} and T_e are the shaft and electromagnetic torque, and f_v is the viscous damping. The J_{sh} is the net shaft inertia, which is the sum of generator inertia J_g and turbine inertia J_t. $\omega_m = d\theta_m/dt$ is the rotor speed, θ_m denotes the measured rotor position bounded to the range $-\pi$ to π. ρ, R_b is the air density and turbine radius. $\mathcal{C}_p$ is the power coefficient, which depends on the TSR $\lambda = \frac{\omega_m R_b}{\mathcal{V}_w}$, where, $\mathcal{V}_w$ is the wind velocity. The MPE of WTS is achieved through OTC by making $T_{\text{sh}} = T_e$. Therefore, the T_e reference should be

$$T_e^* = K_{\text{opt}}\omega_m^2. \tag{3}$$

In which, the OTC constant $K_{\text{opt}} = 0.5\rho\pi R_b^5 \mathcal{C}_p^{\max}/\lambda_{\text{opt}}^3$, where, $\mathcal{C}_p^{\max}$, λ_{opt} are the optimum values [1].

The continuous time mathematical model of PMVG in terms of dq-axes voltages is given as follows:

$$v_d = -r_s i_d + \omega_e L_d i_q - L_d\frac{di_d}{dt} + \underbrace{0}_{e_d} \tag{4}$$

$$v_q = -r_s i_q - \omega_e L_q i_d - L_q\frac{di_q}{dt} + \underbrace{\omega_e\Psi_e}_{e_q} \tag{5}$$

$$T_e = -1.5pi_q\Psi_e \tag{6}$$

where v_d, v_q, i_d, i_q are dq-axes stator voltages and currents, $e_d = 0$, $e_q = \omega_e\Psi_e$ are the dq-axes components of stator induced emf. r_s is the stator resistance, L_d and L_q are the dq inductances, Ψ_e is the magnetic flux linkage, and p denotes the magnetic pole pairs. The angular frequency of induced emf is $\omega_e = p\omega_m = \frac{d\theta_e}{dt}$, where $\theta_e = p\theta_m$ is the electrical equivalent of measured rotor position bounded to the range $-\pi$ to π [20].

B. ZDC-Cascade Control of MSC.

The ZDC-cascade control schematic of PMVG MSC is illustrated in Fig. 1. The MPE operation is realized by the generator torque control by deriving the torque component of stator current $i_q^* = \frac{-T_e^*}{1.5p\Psi_e}$ by using (3) and (6). The i_d^* is set to zero and the phase angle of induced emf θ_e is usually calculated from the encoder-measured rotor position θ_m. Further, the measured stator currents i_{abc} are transformed to dq-axes through abc/dq transformation by employing θ_e. The i_{dq} currents are compared with their references and the errors are processed by PI controllers to generate v_{dq} references. Next, through dq/abc transformation by employing θ_e, the v_{dq}^* are transformed to v_{abc}^*. The space vector pulse width modulation (SVPWM) block generates gating pulses to the MSC to realize these reference stator voltages [20].

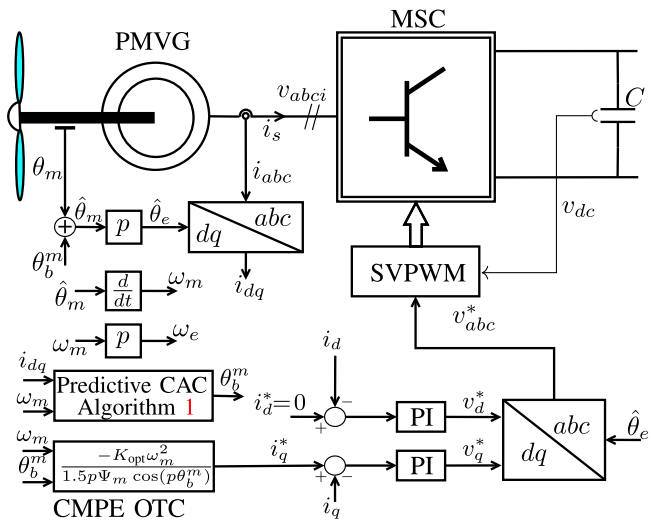

Fig. 1. PMVG ZDC control scheme with FA-RPB-based CAC and CMPE.

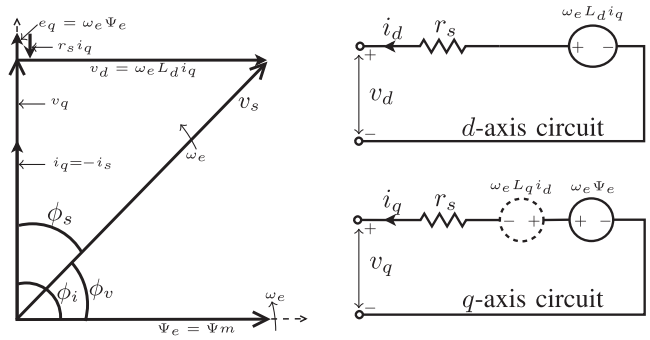

Fig. 2. Space vector diagram of PMVG machine with ZDC control.

C. PMVG Power Factor Analysis

The PMVG space vector diagram under ZDC control operating with the encoder signal derived θ_e is illustrated in Fig. 2. It is drawn with the assumption, that the rotor flux linkage Ψ_e is synchronized with the d-axis of dq reference frame and equal to the maximum flux linkage Ψ_m. The vectors depicted in Fig. 2 are rotating in space with the speed of ω_e, which is the electrical equivalent of the generator rotor speed. The q-axis stator current i_q is perpendicular to the rotor flux Ψ_e and aligned with the e_q. Then, the stator voltage can be derived as follows:

$$v_s = \sqrt{v_d^2 + v_q^2} = \sqrt{(\omega_e L_d i_q)^2 + (\omega_e\Psi_e - r_s i_q)^2}. \tag{7}$$

The phase displacement angle ϕ_s can be written as

$$\phi_s = \phi_v - \phi_i \tag{8}$$

where ϕ_i and ϕ_v are stator current and voltage angle

$$\phi_i = \tan^{-1}\left(\frac{i_q}{i_d}\right); \quad \phi_v = \tan^{-1}\left(\frac{v_q}{v_d}\right). \tag{9}$$

Then, with ZDC control, the i_d is maintained at zero by the PI controller, and the PF angle can be deduced as

$$\phi_s = \tan^{-1}\left(\frac{v_q}{v_d}\right) - \frac{\pi}{2}. \tag{10}$$

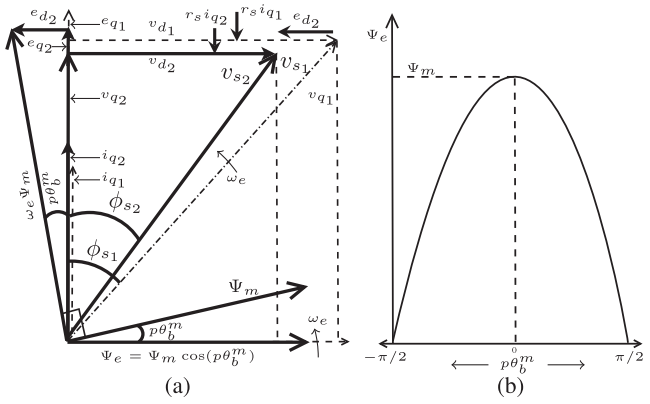

Fig. 3. Modified space vector diagram and magnetic flux variation with CAC.

III. CMPE Under CAC for Power Factor Improvement

A. RPB-Based CAC for PF Improvement

From Fig. 2, the PF can be increased by reducing the angle ϕ_s. Based on (10), it can be achieved by reducing the v_d by advancing the v_s toward the anticlockwise direction. Generally, for MSC ZDC cascade control, the rotor position angle θ_m is used in deriving the parameters ω_m, θ_e. Moreover, a CAC can be employed to introduce a rotor position bias (RPB) parameter θ_b^m [17], [34]. Then, the θ_b^m is added to the θ_m to modify the measured rotor position as $\hat{\theta}_m = \theta_m + \theta_b^m$, which modify the θ_e to a new value $\hat{\theta}_e = \theta_e + p\theta_b^m = p\hat{\theta}_m$. As a result, the i_d tries to deviate from the zero value, which increase the d-axis current error. Consequently, the d-axis PI current controller suitably adjusts the v_d to make the current error zero. The space vector diagram in Fig. 3 comparatively illustrates the various operating vectors before and after introducing the RPB.

The bias value to the rotor position modifies the vectors as depicted in Fig. 3(a) by shifting the vector Ψ_m toward anti-clockwise direction by an angle $p\theta_b^m$. As a result, the amplitude of airgap flux linkage Ψ_e aligned with d-axis is reduced to $\Psi_m \cos(p\theta_b^m)$. Fig. 3(b) illustrates the relationship between the bias angle and airgap magnetic flux linkage Ψ_e. Accordingly, the e_d changes from zero to e_{d_2} for the introduced –ve bias angle $\theta_b^e = p\theta_b^m$. Therefore, based on (4), (5), the amplitude of v_d changes from v_{d_1} to v_{d_2}, and the amplitude of v_q changes from v_{q_1} to v_{q_2}. In addition, regarding the PMVG operation, based on (6), the electromagnetic torque developed is modified to

$$T_e = -1.5p\Psi_m \cos(p\theta_b^m) i_q. \tag{11}$$

On this account, the reduction in T_e by the factor $\cos(p\theta_b^m)$ affects the dynamics of rotor speed based on (2). Therefore, the rotor speed is momentarily increased. As a result, based on (3) and (6), the i_q^* is eventually increased. Consequently, the parameters $i_{q_1}, e_{q_1}, \phi_{s_1}, v_{s_1}$ are changed to $i_{q_2}, e_{q_2}, \phi_{s_2}, v_{s_2}$. Moreover, the adjustment to v_{dq} by the RPB θ_b^m is carried by altering the references v_{dq}^*, v_{abc}^* to the SVPWM generation unit by the action of PI controller. As a result, the MSC adjusts the stator voltage to advance a considerable angle. Finally, with the suitable –ve RPB θ_b^m, the PF can be increased by reducing the angle ϕ_s from ϕ_{s_1} to ϕ_{s_2}. Similarly, a +ve bias value does the opposite action by shifting the vectors toward the clockwise direction and eventually reduces the PF by increasing the ϕ_s.

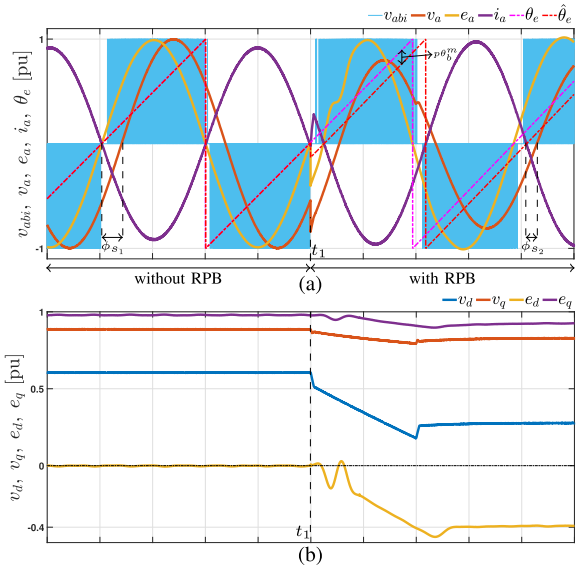

Fig. 4. Steady state responses with and without RPB. (a) Stationary frame variables in pu. (b) dq-frame variables in pu.

Fig. 4 comparatively illustrates the steady-state responses of PMVG with and without RPB, for which the θ_b^m is assumed as the CAC-derived bias angle. The stationery frame responses of MSC line-to-line voltage v_{abi}, estimated fundamental induced emf e_a (based on Abdelrahem et al.'s [33] work), estimated fundamental phase voltage v_a, and phase current i_a are depicted in Fig. 4(a). Until the instant t_1, the RPB θ_b^m is kept as zero ($\hat{\theta}_m = \theta_m$). Then, at instant t_1, the CAC is enabled and the –ve bias θ_b^m is added to the measured rotor position, therefore the $\hat{\theta}_m = \theta_m + \theta_b^m$, and $\hat{\theta}_e = \theta_e + p\theta_b^m$. From the response plot, it is obvious that, the $\hat{\theta}_e$ under CAC-derived RPB is delayed by a considerable angle. As a result, the PF angle ϕ_s under RPB is modified from ϕ_{s_1} to ϕ_{s_2}, thereby achieving the improvement in stator PF. Also, the influence of CAC-derived RPB over the parameters e_a, v_a are much evident from the responses. In addition, the rotating reference frame responses v_d, v_q, e_d, e_q for the additional bias θ_b^m is illustrated in Fig. 4(b). Initially, until the instant t_1, the e_d is aligned to zero under the measured rotor position-derived current angle $\hat{\theta}_e = p\theta_m$. Then, after t_1, the e_d is changed to -0.4 pu due to the modified current angle $\hat{\theta}_e = p\theta_m + p\theta_b^m$. Consequently, as illustrated in the vector diagram Fig. 3(a), the lag angle between v_s and i_s is adjusted to improve the PF.

Remark 1: The RPB θ_b^m for CAC modifies the parameter e_d and influences other variables as explained earlier. In this context, the approximate relationship between the θ_b^m and v_q, v_d can be derived by using (3)–(6), (11), Fig. 3 under the assumption that the r_s is negligible, ω_e is maintained constant, and the $\frac{di_d}{dt} = \frac{di_q}{dt} = 0$

$$v_d(\theta_b^m) = \frac{\omega_e L_d K_{\text{opt}} \omega_m^2}{1.5p\Psi_m \cos(p\theta_b^m)} - \omega_e \Psi_m \sin(p\theta_b^m) \tag{12}$$

$$v_q(\theta_b^m) = \omega_e \Psi_m \cos(p\theta_b^m). \tag{13}$$

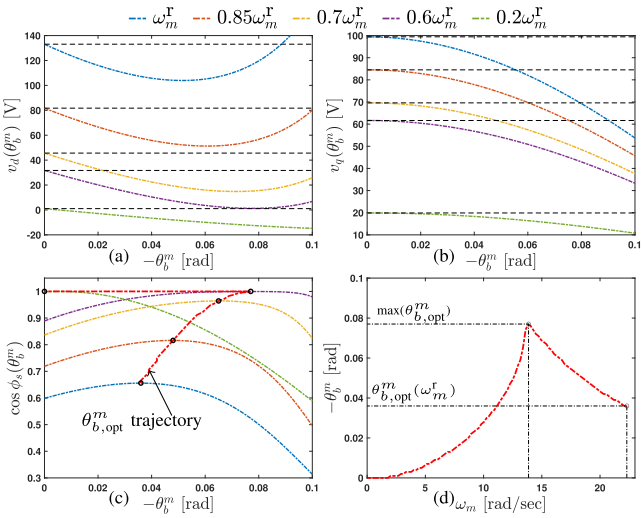

Fig. 5. Analytical responses of 5-kW PMVG for varying RPB θ_b^m under different operating speed. (a) $v_d(\theta_b^m)$. (b) $v_q(\theta_b^m)$. (c) Power factor and optimum θ_b^m trajectory. (d) Rotor speed versus optimum θ_b^m.

TABLE I
PMVG PARAMETERS

Description	Parameter	Value	
		Experiment [1]	Simulation [36]
Rated rotor speed	ω_m^r	22.06 rad/s	1.496 rad/s
Rated emf/phase	e_s	71 V	451.9 V
Rated current	i_s	23.6 A	1216.8 A
Stator resistance	r_s	0.44 Ω	15.7 mΩ
Stator inductance	L_s	17.5 mH	6.2 mH
Flux linkage	Ψ_m	0.4459 Wb	5.9247 Wb
Pole pairs	p	10	70
Moment of inertia	J_g	0.18 kg-m^2	64872 kg-m^2
Rated output power	P_e^r	5 kW	1.6 MW

Based on (12) and (13), for a given rotor speed ω_m, the $v_d(\theta_b^m)$, $v_q(\theta_b^m)$ exhibits a nonlinear behavior. Fig. 5 illustrates the v_d, v_q, $\cos\phi_s$, and rotor speed versus optimum θ_b^m analytical responses using (12), (13), and (10) for a 5-kW PMVG parameters listed in Table I. From the response plot in Fig. 5(a), for any fixed rotor speed ω_m the v_d start to decrease first until a particular point and increases again with the increase in θ_b^m. Besides, the v_q is decreasing continuously with an increase in θ_b^m, as shown in Fig. 5(b). The resultant change in PF and the trajectory of optimum θ_b^m for maximum PF is illustrated in Fig. 5(c). From this, it is obvious that the PF can be increased to unity for operating speeds $< 0.6\omega_m^r$ by properly selecting the RPB θ_b^m. Further, for operating speeds $> 0.6\omega_m^r$, the PF cannot be increased to unity, however can be increased from the typical value.

Moreover, the optimum θ_b^m is unique for each of the rotor speeds to ensure the maximum PF, which is illustrated for the considered 5-kW rated PMVG in Fig. 5(d). Any increment beyond those unique θ_b^m will lead to reduction in PF and its effect over the other operating parameters is counter-productive. Therefore, the range of θ_b^m has hard limitations which depend on various factors, such as magnetic saturation properties of the machine, current rating, variation in inductance, and other operating parameters. Regarding the 5-kW PMVG parameters in Table I, the hard limit to the θ_b^m can be selected as –0.08. Any bias value beyond this limit will not increase the PF under any operating speed, rather the PF will start to reduce and severely affect other operating parameters.

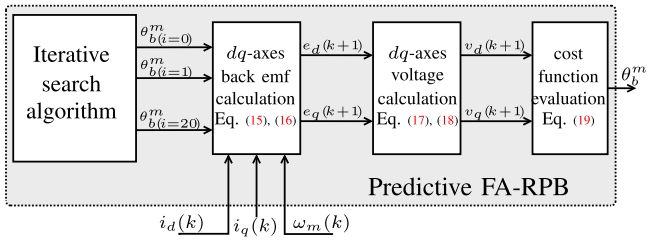

Fig. 6. Proposed predictive FA-RPB scheme block diagram.

Algorithm 1: FA-RPB for current angle control.

Step 1: Get $i_d(k)$, $\omega_m(k)$, $i_q(k)$.
Step 2: Set $\theta_{b,\text{opt}}^m = 0$, and $g_{\text{opt}} = 0$.
Step 3: Begin FA-RPB estimation.
  for $i = 0:1:20$ **do**
    Calculate $\theta_{bi}^m = -0.004 \times i$;
    Calculate $e_{dqi}(k+1)$ using (15), (16);
    Calculate $v_{dqi}(k+1)$ using (17), (18);
    Calculate g_i using (19);
    Maximize g_i
    if abs$(g_i) > g_{\text{opt}}$ **then**
      $g_{\text{opt}} = \text{abs}(g_i)$, and $\theta_{b,\text{opt}}^m = \theta_{bi}^m$;
    end if
  end for
Step 4: Set optimum RPB $\theta_b^m = \theta_{b,\text{opt}}^m$.

B. Proposed FA-RPB-Based CAC for PF Improvement

As outlined in the Remark 1, the optimum θ_b^m is unique for each of the rotor speeds. Moreover, the nonlinear relationship between the RPB θ_b^m and the PF makes it difficult to formulate a conventional closed-loop CAC to ensure the maximum PF and hard limit constraints. Therefore, the idea of FA-RPB is established based on the FCS-MPC principle. The FCS-MPC utilizes a finite number of converter switching states to predict the possible future behavior of various operating parameters over a prediction horizon. Then, an optimum switching state that optimizes a specific cost function is selected as the optimum one and applied in the next instruction cycle of the controller [37]. The block diagram of the proposed FA-RPB is illustrated in Fig. 6 and the iterative search method is formulated as Algorithm 1.

The FA-RPB-based CAC is formulated as an iterative search algorithm to find the optimum RPB for PF improvement. The range of RPB from zero to the maximum limit is discretized into a finite number of angles and applied to the v_d, v_q discrete models to predict the PF for each of the finite bias angles. Then, based on the cost function maximization, one optimum RPB is identified and applied to the next instruction cycle.

The algorithm begins by reading the actual values $\omega_m(k)$, $\omega_e(k)$, $i_d(k)$, and $i_q(k)$ from the MSC vector control. Then the

RPB θ_b^m and cost function g_{opt} is initialized to zero. Next, in order to get the discrete bias angles, an iterative searching loop with index i is used. The total number of iterations for the loop is obtained as the ratio of the RPB range to the step increment in RPB for each iteration plus one. Therefore, for the hard limit –0.08 and discrete step increment –0.004, the total number of iterations is selected as 21. Next for each iteration, the discretized RPB θ_{bi}^m is calculated as follows:

$$\theta_{bi}^m = -0.004 \times i. \tag{14}$$

Next, the electrical equivalent of RPB is calculated as $\theta_{bi}^e = p\theta_{bi}^m$, and the $e_{dqi}(k+1)$ are predicted for the θ_{bi}^e by using the following discrete dynamics derived from Fig. 3:

$$e_{di}(k+1) = \sqrt{(\omega_e(k)\Psi_m)^2 - (\omega_e(k)\Psi_m \cos(p\theta_{bi}^m))^2} \tag{15}$$

$$e_{qi}(k+1) = \omega_e(k)\Psi_m \cos(p\theta_{bi}^m). \tag{16}$$

Then, the v_{dqi} voltages are predicted by the following derived discrete models from (4) and (5):

$$v_{di}(k+1) = -r_s i_d(k) - \omega_e(k) L_d i_q(k) + e_{di}(k+1) \tag{17}$$

$$v_{qi}(k+1) = -r_s i_q(k) + \omega_e(k) L_q i_d(k) + e_{qi}(k+1). \tag{18}$$

Then, the following cost function is defined to approximate the predicted PF for assumed RPB θ_{bi}^m:

$$g_i = \cos\left\{\tan^{-1}\left\{\frac{v_{qi}(k+1)}{v_{di}(k+1)}\right\} - \frac{\pi}{2}\right\}. \tag{19}$$

Next, the RPB that maximizes the cost function is selected as the optimum RPB θ_b^m after 21 iterations of the index i. The predicted RPB is then passed to the low pass filter and added to the measured rotor position.

Note 1: The Algorithm 1 identifies the optimum RPB for PMVG PF improvement by considering the dynamic properties of the PMVG. However, regarding the WTS operation, the additional RPB added to the measured rotor position alters the generator variables. It also affects the MPE operation due to the modified T_e based on (11). Moreover, the effect of θ_b^m over the generator T_e is obvious from Fig. 3(b). As a consequence, the deviation between the T_{sh} and T_e increases and the rotor speed ω_m reaches a new steady state value based on (2) and (3). Therefore, the ω_m increases beyond the optimum value, as a result, the wind turbine operating speed becomes suboptimal. Hence, based on the aerodynamic model of WTS, the λ and C_p deviate, respectively, from λ_{opt} and $C_p^{\max}$. Consequently, there will be a noticeable reduction in aerodynamic power extraction under PF improvement with the introduction of θ_b^m.

C. CMPE Operation

Therefore, to deal with the concern of reduction in T_e and consequent reduction in aerodynamic power extraction as outlined in Note 1, the rotor speed should be maintained at the optimum value even after the introduction of θ_b^m. From the previous analysis, it is understood, that the reason for the perturbation in rotor speed due to the introduction of θ_b^m is the reduction in T_e by the factor $\cos(p\theta_b^m)$ [based on (11)]. Therefore, a suitable increment in T_e to compensate for this effect is necessary. Consequently, an RPB parameter-constrained MPE can be formulated by redesigning the i_q^* of MSC cascaded control. Accordingly, the required increment in T_e is derived by relating the (3) and (11). Thereby, the CMPE is achieved by redesigning the i_q^* of OTC control as follows:

$$i_q^* = \frac{-K_{\text{opt}}\omega_m^2}{1.5p\Psi_m \cos(p\theta_b)}. \tag{20}$$

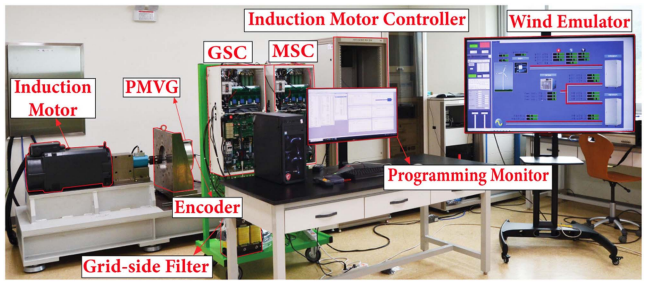

Fig. 7. Laboratory experimentation setup of 5-kW PMVG-based WTS.

TABLE II
WTS AND MSC CONTROL PARAMETERS

Description	Parameter	Value	
		Experiment [39]	Simulation
Rated wind speed	$\mathcal{V}_w^{\text{r}}$	9 m/s	9.7 m/s
WTS radius	R_b	2.82 m	44.6 m
Rated power	P_{ad}^{r}	5 kW	1.6 MW
Moment of inertia	J_t	1 kg-m^2	48e^5 kg-m^2
Optimum TSR	λ_{opt}	6.912	6.912
Max. power coefficient	$C_p^{\max}$	0.4412	0.458
dc-link voltage	v_{dc}	350 V	2200 V
Switching frequency	f_{sw}	10 kHz	3 kHz
OTC constant	K_{opt}	0.459	470960
q-axis CC PI gains	K_{p_q}, K_{i_q}	2.5, 25	0.24, 3.7
d-axis CC PI gains	K_{p_d}, K_{i_d}	2, 25	0.24, 3.7

IV. METHOD VALIDATION

In this section, the proposed FA-RPB-based CAC for PF improvement has been validated by implementing it in a two-level converter fed 5-kW rated PMVG driven by a wind turbine emulator. Fig. 7 shows the PMVG WTS experimental setup, the generator specifications are listed in Table I, the WTS, MSC, and CC parameter specifications are given in Table II. The MSC converter is configured with three Fuji Electric 2MBI100VA-120-50 IGBT switching modules each containing two series connected IGBT devices. A 415 μF, 1100 V/60 A rated electrolytic capacitor is used as a dc-link. The MSC vector control strategy is executed on a dedicated Texas Instruments TMS320F28335 digital signal processor with a 10 kHz sampling frequency. The processor produces the complementary PWM pulses with 3μs dead-time and applied to the IGBT switching devices through the Realtech two-level gate interface board. Further, LEM LV 25-P voltage transducers measure the machine and dc-link capacitor voltages. Besides, LEM HAS 50-S current transducers are used to measure the machine currents. The Autonics E40S6-1024-6-L-5 rotary-type incremental encoder measures the rotor position for rotor speed calculation and MSC vector control formulation.

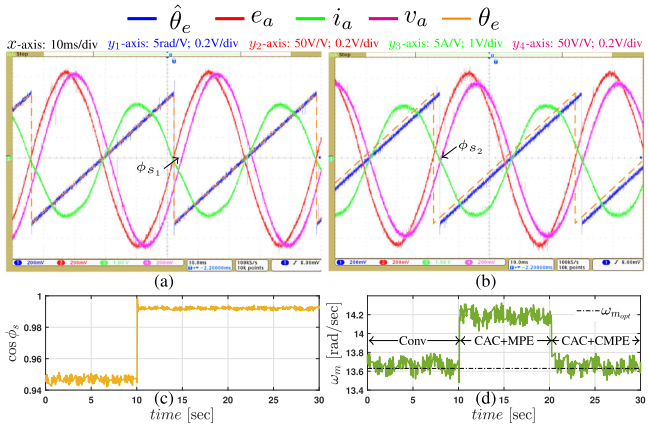

Fig. 8. MSC experimental responses with $0.6\omega_m^{\mathrm{r}}$. (a) Without CAC. (b) With CAC. (c) PF improvement. (d) ω_m deviation.

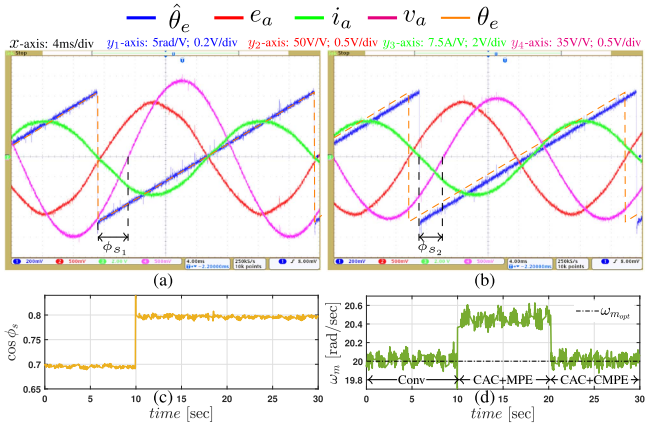

Fig. 9. MSC experimental responses with $0.9\omega_m^{\mathrm{r}}$. (a) Without CAC. (b) With CAC. (c) PF improvement. (d) ω_m deviation.

The OTC principle described in Section II regulates the rotor speed for MPE operation. The MSC cascaded control in Fig. 1 is formulated based on the vector control approach described in Palanimuthu et al.'s [38] work. The execution time of the entire control system with presented FA-RPB-based CAC scheme accounts to 40 μs, which can be easily handled by the DSP in a control cycle. This includes the signal measurement, filtering, data processing/monitoring, fault detection, and SVPWM generation algorithms. Particularly, the presented FA-RPB-based CAC iterative program (Algorithm 1) takes an execution time $< 8\mu$s, which is a reasonable computation allocated by the controller for the PF improvement. The experiment is carried out in three cases as follows.

1) Conventional method without PF improvement ($\theta_b^m = 0$).
2) FA-RPB-based CAC with conventional MPE.
3) FA-RPB-based CAC with CMPE.

A. Steady State Experimentation Result

The steady-state experimentation is carried out by maintaining a constant wind velocity for 30 s. In which, until $t = 10$ s, the WTS is operated with conventional MPE without enabling the CAC ($\theta_b^m = 0$ rad), then for the duration $t = 10$–20 s, the CAC is enabled by applying the RPB, therefore the WTS is operating with CAC+MPE for PF improvement. Afterward, at $t = 20$ s, the CMPE is enabled by modifying the i_q^* as (20).

First, the WTS has operated with a wind velocity of 5.5 m/s and the $[e_a\ v_a\ i_a\ \hat{\theta}_e]$, $\cos\phi_s$, ω_m responses are shown in Fig. 8, for which the optimum rotor speed $\omega_{m_{\mathrm{opt}}} = 0.6\omega_m^{\mathrm{r}}$. The responses of $[e_a\ v_a\ i_a\ \hat{\theta}_e]$ under without CAC ($\theta_b^m = 0$ rad) in Fig. 8(a) reveal that, the v_a is displaced by an angle ϕ_{s_1} from the e_a, and the i_a has an exact phase displacement π rad from e_a. Therefore, the usage of derived rotor position $\hat{\theta}_e = \theta_e$ in cascade control leads to a PF $\cos\phi_{s_1} = 0.94$. Then, Fig. 8(b) illustrates the $[e_a\ v_a\ i_a\ \hat{\theta}_e]$ responses after enabling the CAC at $t = 10$ s by applying the RPB $\theta_b^m = -0.04$ rad. The application of θ_b^m modifies the i_a current angle, consequently, the displacement between the v_a and i_a is reduced to ϕ_{s_2} and the $\cos\phi_s$ is increased to 0.995. Moreover, the improvement in PF is illustrated in Fig. 8(c). Besides, the application of RPB at $t = 10$ s modifies the T_e (11). As a result, the rotor speed deviates from the optimum value, as shown in Fig. 8(d). Further, the enabling of CMPE operation at $t = 20$ s modifies the T_e, consequently, the rotor speed is again made to track the $\omega_{m_{\mathrm{opt}}}$. Therefore, the power factor-improvement-constrained MPE operation is verified.

Next, the steady-state responses are illustrated in Fig. 9 for a wind velocity 8.1 m/s (90% of $\mathcal{V}_w^{\mathrm{r}}$), for which the $\omega_{m_{\mathrm{opt}}} = 0.9\omega_m^{\mathrm{r}}$. The $[e_a\ v_a\ i_a\ \hat{\theta}_e]$ responses under without CAC and with CAC are illustrated respectively in Fig. 9(a) and (b). As explained in Remark 1, the PMVG PF cannot be made unity for $\omega_m > 0.6\omega_m^r$, however, it can be improved from the nominal value. Accordingly, the enabling of CAC with RPB $\theta_b^m = -0.04$ rad modifies the phase displacement angle from ϕ_{s_1} to ϕ_{s_2}. Besides, the improvement in PF is illustrated in Fig. 9(c), and the rotor speed responses with conventional, CAC+MPE, CAC+CMPE is pictured in Fig. 9(d).

B. Dynamic Response With Step-Varying Wind Profile

The practical applicability of the proposed FA-RPB for CAC and CMPE is verified under two different cases of exponentially smoothened step-varying wind profile. In case-1 wind profile, the WTS optimum rotor speed ranges from $0.5\omega_m^{\mathrm{r}}$ to ω_m^{r}. Next, the case-2 wind profile is considered for low speed operation range $0.3\omega_m^{\mathrm{r}}$–$0.6\omega_m^{\mathrm{r}}$.

1) Case-1: The experimental responses are comparatively illustrated in Fig. 10. The rotor speed responses in Fig. 10(a) show that the CAC+MPE scheme deviates the rotor speed from $\omega_{m_{\mathrm{opt}}}$ due to the enabling of FA-RPB for PF improvement. This is due to the modified PMVG T_e modeled in (11). However, the CAC+CMPE ensures the optimum rotor speed operation as like the conventional method in response to the modified i_q^* in (20). Besides, the TSR responses illustrated in Fig. 10(b) show that the CAC+MPE scheme operates with a suboptimal operating point but the CAC+CMPE scheme ensures the λ to its optimal value. The PMVG i_{dq} responses are pictured in Fig. 10(c) and the modification in T_e is illustrated in Fig. 10(d). Consequently, the maximum stator active power P_e under CAC+CMPE is ensured, as depicted in Fig. 10(e). On the other hand, the stator reactive power S_e under CAC+MPE is significantly reduced because of

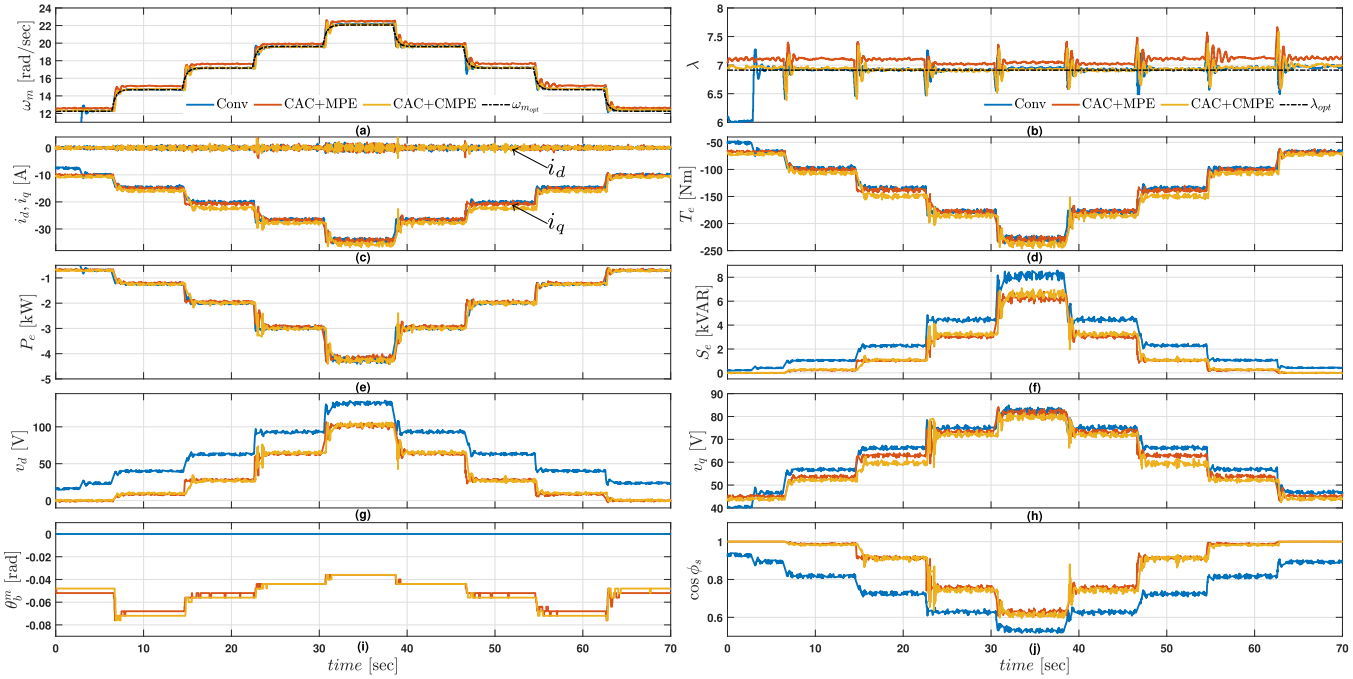

Fig. 10. Experimentation results with step-varying wind profile case-1. (a) Rotor speed. (b) TSR. (c) dq-axes current. (d) Electromagnetic torque. (e) PMVG stator active power. (f) PMVG stator reactive power. (g) d-axis voltage. (h) q-axis voltage. (i) Optimum RPB. (j) Power factor.

the reduction in the current lag angle due to the introduction of RPB. However, the CMPE operation slightly increases the S_e but is still significantly lower than the conventional method, as pictured in Fig. 10(f).

Next, the v_d response in Fig. 10(g) justifies the reduction in its amplitude under the CAC+MPE scheme, which is the reason for the reduction in PF angle ϕ_s. However, the CMPE slightly alters the v_d behavior, still holds a great deal of reduction in amplitude. Further, the v_q response in Fig. 10(h) shows the effect of CAC over its amplitude which indirectly affects the rotor speed. On the other side, the CMPE scheme suitably adjusts the v_q and nullifies the ω_m deviation and ensures the MPE operation. Next, the optimum bias angle applied to the CC by the FA-RPB scheme is pictured in Fig. 10(i). In which, the bias angle θ_b^m is developed in multiples of –0.004 based on (14). Moreover, under conventional MPE control, the θ_b^m is zero. For CAC+MPE and CAC+CMPE, the –ve θ_b^m is introduced as an RPB to improve the PF. The optimum θ_b^m under CAC+MPE and CAC+CMPE slightly differs due to the difference in rotor speed. In addition, considerable oscillations in bias value can be noted at the time of wind speed transients due to the oscillatory rotor speed response. Then, Fig. 10(j) portrays the improvement in PF under FA-RPB-based CAC+MPE and CAC+CMPE methods as compared to the conventional MPE method.

2) Case-2: The experimental responses under low speed operation is pictured in Fig. 11. The ω_m responses are illustrated in comparison with the conventional scheme in Fig. 11(a). The rotor speed under the CAC+MPE scheme deviates from the optimal speed when operating around 0.6 times the rated speed (13–15 rad/s). This deviation is attributed to the RPB applied by the Algorithm 1 approaching its maximum allowable value

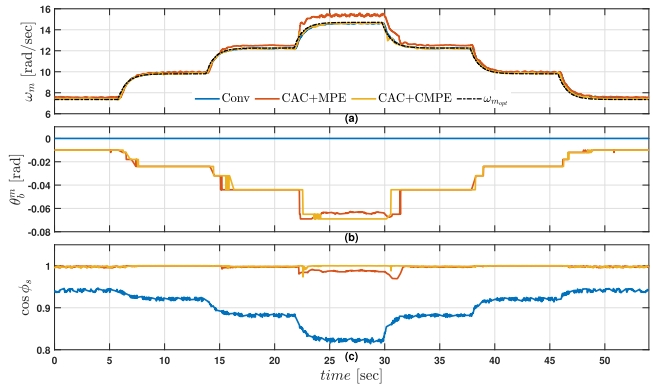

Fig. 11. Experimentation results with step-varying wind profile case-2. (a) Rotor speed. (b) Optimum RPB. (c) Power factor.

(max$\{\theta_{b,\text{opt}}^m\}$), as illustrated in Fig. 5(d). However, the CMPE effectively compensates this deviation, ensuring operation at the desired speed. Next, the experimentally observed RPB in Fig. 11(b) closely matches with the analytical optimum RPBs. The PF responses are pictured in Fig. 11(c), the FA-RPB scheme maintains a PF of nearly unity up to $0.6\omega_m^r$, significantly outperforming the conventional scheme, which exhibits a comparatively lower PF. This confirms the accuracy of the presented approach for determining optimal RPB settings.

C. Dynamic Response With Random-Varying Wind Profile

Next, the experimental verification of proposed FA-RPB scheme is extended to the random-varying wind profile and the responses are illustrated in Fig. 12. The rotor speed responses

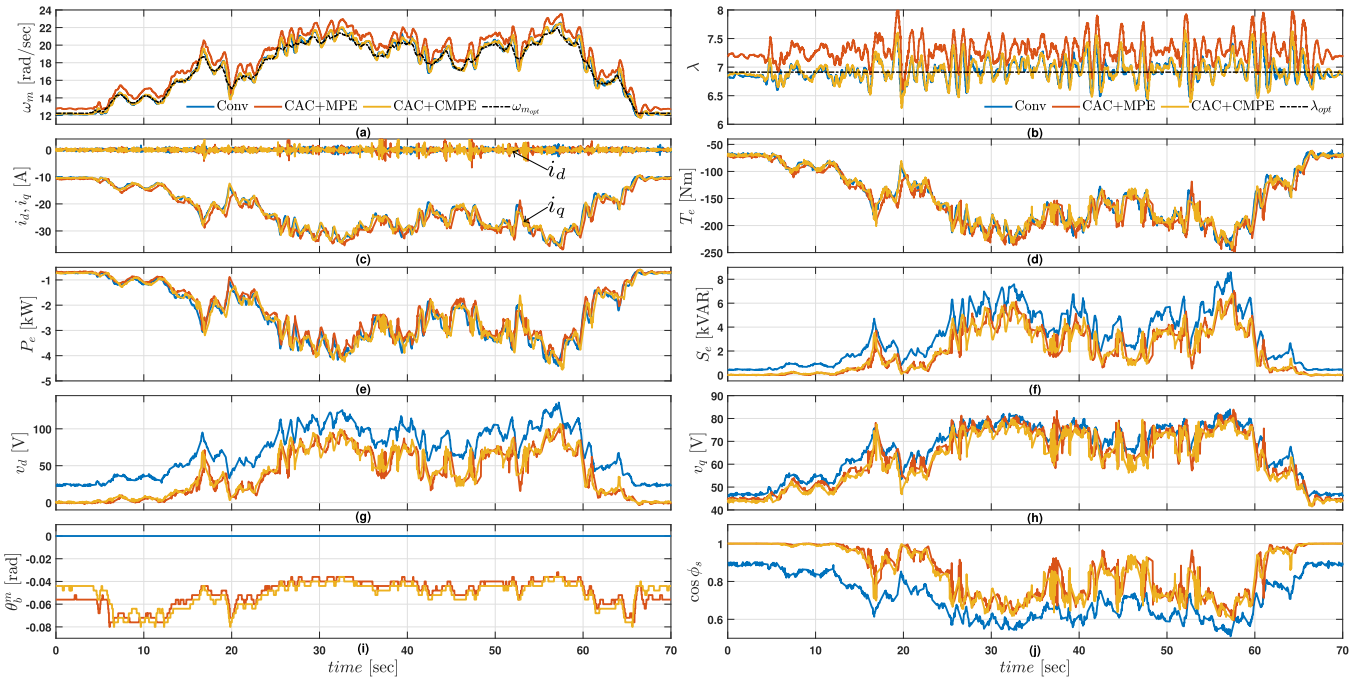

Fig. 12. Experimentation results with randomly varying wind profile. (a) Rotor speed. (b) TSR. (c) dq-axes current. (d) Electromagnetic torque. (e) PMVG stator active power. (f) PMVG stator reactive power. (g) d-axis voltage. (h) q-axis voltage. (i) Optimum RPB. (j) Power factor.

are plotted in Fig. 12(a) and the TSR responses are illustrated in Fig. 12(b). In which, the CAC+MPE scheme operates with a suboptimal operating point, however the CAC+CMPE scheme ensures the WTS operation in the optimal rotor speed and TSR. Then, the PMVG i_{dq} and T_e responses are illustrated in Fig. 12(c) and (d). Next, the stator active power and reactive power responses are illustrated, respectively, in Fig. 12(e) and (f). Besides, Fig. 12(g) and (h) potrays the dq-axes voltages under conventional, CAC+MPE, and CAC+CMPE schemes. Further, the FA-RPB algorithm developed RPB is pictured in Fig. 12(i), which shows that, the θ_b^m is introduced in multiples of –0.004 and varying with the rotor speed ω_m. The consequent improvement in PF is illustrated in Fig. 12(j). From the response of PF, it is verified that the PMVG operating PF is brought to unity until the $\omega_m = 0.6\omega_m^{\mathrm{r}}$. Further, for operating speeds $\omega_m > 0.6\omega_m^{\mathrm{r}}$, the stator PF is improved from the typical value. Therefore, the effectiveness of the proposed FA-RPB-based CAC scheme for PF improvement is verified.

Remark 2: From the dynamic responses with step-varying and random-varying wind profiles, it is observed that, the PMVG stator PF is less than unity for below rated speed operations. Further, with rated operating speed, the PF is quantified as around 0.5. This is a typical PF for the PMVGs due to their leakage flux, magnetic gearing effect and other design considerations. However, with the presented scheme the stator PF is brought to unity until the $0.6\omega_m^{\mathrm{r}}$, and improved from its typical values for the operating speed range $0.6\omega_m^{\mathrm{r}}$–ω_m^{r}. Therefore, the presented scheme enhances the robustness of PMVGs in WTS applications.

Note 2: The proposed FA-RPB scheme (Algorithm 1) experimental implementation considers -0.004 as incremental step size, as discussed in Section III-B (14). This approximation is based on the analytically identified θ_b^m hard-limit and selected iteration count 21. The incremental step size can be further reduced with increased iteration count; as a result, a smooth RPB is generated to reduce the oscillations in PF. However, the increased iteration count will require additional computation. Therefore, the iteration count for the FA-RPB-based Algorithm 1 should be carefully selected by the user by considering the computational resource in the digital controller.

D. Comparative Performance Analysis

1) With Different Hard Limit Settings: The analytical response in Fig. 5 reveals that, the increase in RPB beyond –0.08 will negatively impact PF. To maintain optimal performance, the FA-RPB algorithm enforces –0.08 as the maximum allowable RPB. The Algorithm 1 increments the index i from 0 to 20 with the step size –0.004 to ensure RPB exploration within the –0.08 limit. Finally, the presented FA-RPB algorithm identifies the optimum RPB among the 21 RPBs with the constraint to maximize the PF. With this background, for the hard limits beyond –0.08 with the proportionally increased iteration count and similar step size, the presented algorithm identifies same θ_{bi}^m as the optimum. This is because the RPB beyond –0.08 are not optimal for the considered 5-kW rated parameters. While –0.08 is the hard limit for RPB, we investigated the algorithm's performance under lower hard limits to assess potential benefits. In this context, a comparative experimental test case with four hard limits [HL1 HL2 HL3 HL4] = [–0.02 –0.04 –0.06 –0.08] has been conducted for the entire speed range and the responses are pictured in Fig. 13. To do this, the iteration count is kept at 21 and the incremental step size for each case is calculated

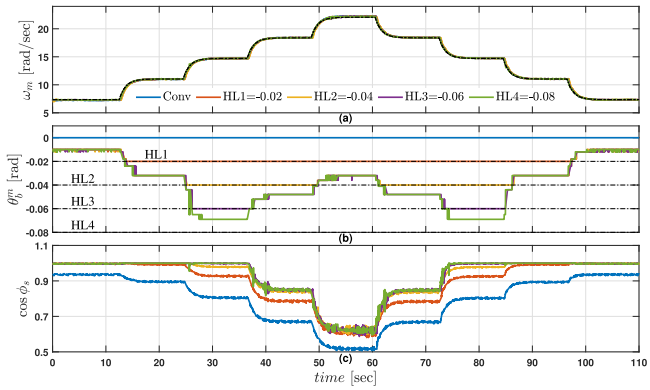

Fig. 13. Experimentation results with different hard limit settings. (a) Rotor speed. (b) Optimum RPB. (c) Power factor.

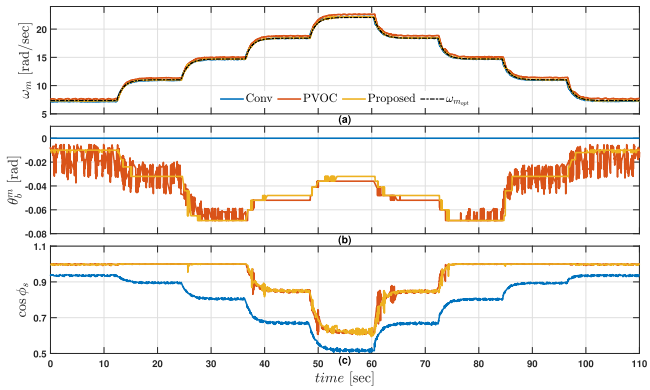

Fig. 14. Comparison with traditional PF improvement scheme. (a) Rotor speed. (b) Optimum RPB. (c) Power factor.

as $\frac{\text{hard limit}}{\text{iteration count - 1}}$, resulting to step sizes [–0.001 –0.002 –0.003 –0.004].

The comparative ω_m responses illustrated in Fig. 13(a) remains optimum across the operating range. The identified optimum RPBs vary depending on the hard limits, as pictured in Fig. 13(b). For the actual optimum RPB lie beyond the assumed hard limits, the hard limit itself is taken as the optimum output (for HL1, HL2, HL3). This arises because the maximum RPB converge to the optimum PF among the discretized RPBs. For HL4, the optimum RPB is within –0.08, the Algorithm 1 identifies the true optimal RPB, further validating the effectiveness in maximizing the PF. The improvement in PF is comparatively demonstrated in Fig. 13(c).

2) Comparison With Traditional PF Improvement Scheme: In this section, the presented scheme has been compared with the phase voltage oriented control (PVOC) [17]. The PVOC forces stator currents to be in phase with the three-phase generator voltages. This approach uses a PI controller with a zero d-axis voltage as its objective, achieved by adjusting the RPB. Therefore, the $(0 - v_d^*)$ is employed as the error signal to the PI controller to evaluate the RPB. However, applying PVOC directly to PMVG has limitations due to their inherent characteristics. Unlike PMSGs, PMVGs cannot maintain a zero d-axis voltage across their entire operating range (see Remark 1 and Fig. 5). To address this, a modified PVOC scheme for PMVGs incorporates a speed-dependent RPB limit function through a look-up table. This limit function, derived from rotor speed constraints in Fig. 5, restricts the maximum allowable RPB based on the operating speed. This ensures optimal performance throughout the PMVG's operating range while preventing limitations of the original PVOC method.

The experimental response of presented scheme is compared with the PVOC and conventional control with no RPB case in Fig. 14. Since the PVOC does not account the T_e modifications due to the introduced RPB in its MPE operation, the rotor speed deviates from the optimum. Besides, the presented scheme ensures the optimum rotor speed throughout the operation, the responses are pictured in Fig. 14(a). Next, from the RPB responses in Fig. 14(b), the PVOC RPB oscillates significantly before reaching its speed-constrained limit, whereas the presented FA-RPB scheme delivers a smooth and stable response. Both schemes achieve comparable PF improvement as in Fig. 14(c), however the transients in presented scheme is minimum with more robust performance. The look-up table evaluation in PVOC is offline and may lead to errors due to variations in operating conditions. The presented scheme dynamically evaluates RPB across the entire operating range, making it adapt online with the unforeseen conditions.

E. Applicability to MW Class PMVG Machines

To verify the scheme's effectiveness in megawatt-scale applications, a simulation case study is conducted using a 1.6-MW PMVG with parameters, as listed in Table I. The wind turbine model incorporates an adjusted $\lambda - C_p$ relationship to adapt with the specifications. Optimum WTS and control parameters for this MW-rated application are summarized in Table II. Following the analytical approach outlined in Remark 1, we obtained responses for v_d, v_q, $\cos\phi_s$, and rotor speed as functions of optimal θ_b^m. These results reveal that, for operating speeds below $0.54\omega_m^{\text{r}}$, PF can be enhanced to near unity by judicious selection of the RPB. For speeds exceeding $0.54\omega_m^{\text{r}}$, PF improvement beyond typical values is achievable. The hard limit for θ_b^m, calculated based on the 1.6-MW PMVG parameters, is determined to be -0.012.

Then, the FA-RPB in Algorithm 1 is programmed as a MATLAB function in the simulink model to evaluate the optimum θ_b^m. Unlike the experimental verification, the simulation provides the computational freedom to select the increased iteration count. Therefore, the iteration count is selected as 101 and by utilizing the calculated θ_b^m hard limit –0.012, the incremental step-size is employed as $\frac{-0.012}{100} = -0.00012$. As a result, a smooth RPB value is taken as the optimum bias, consequently, a smooth response is guaranteed in PMVG PF. To assess performance under changing wind conditions, we simulated the system using a step-varying wind profile. The resulting responses are depicted in Fig. 15.

Similar to the 5-kW rated prototype machine, the CAC+MPE deviates the rotor speed from $\omega_{m_{\text{opt}}}$ as pictured in Fig. 15(a), however, the CAC+CMPE ensures the optimum rotor speed operation. Besides, the TSR responses are illustrated in Fig. 15(b). Next, Fig. 15(c) illustrates the i_d, i_q responses under the

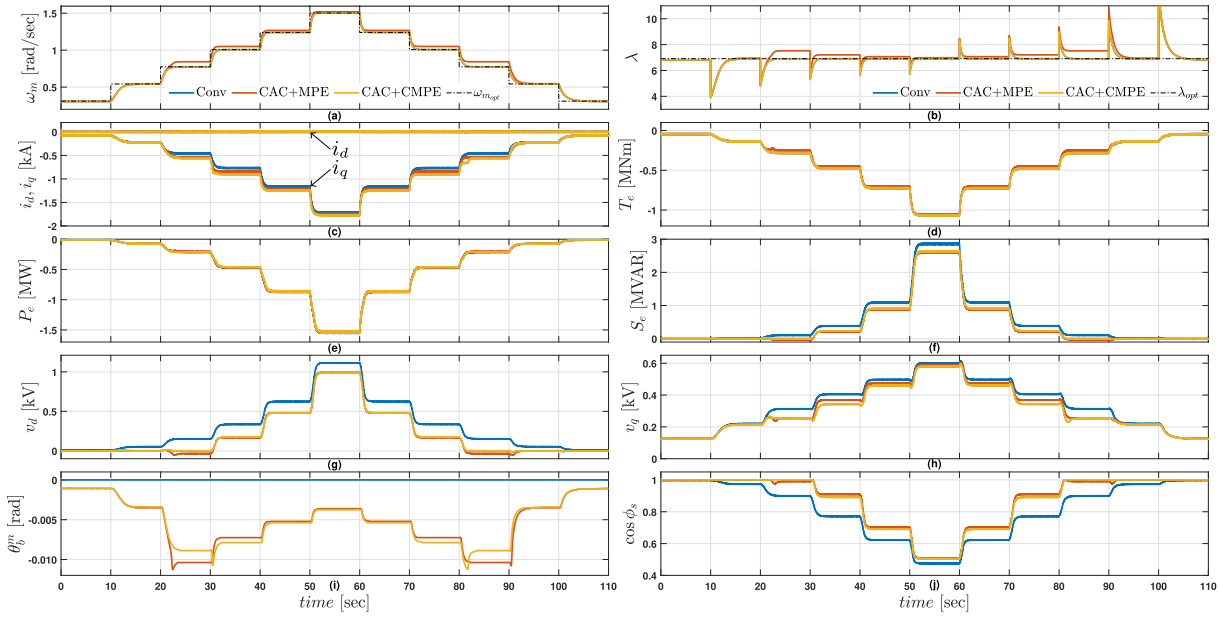

Fig. 15. MW rated simulation results with step-varying wind profile. (a) Rotor speed. (b) TSR. (c) dq-axes current. (d) Electromagnetic torque. (e) PMVG stator active power. (f) PMVG stator reactive power. (g) d-axis voltage. (h) q-axis voltage. (i) Optimum RPB. (j) Power factor.

conventional and modified schemes. The modified PMVG T_e in (11) is clearly differentiated from the conventional scheme in Fig. 15(d). Consequently, maximum stator active power P_e under CAC+CMPE is ensured, as depicted in Fig. 15(e). On the other hand, the stator reactive power S_e under CAC+MPE and CMPE operation is reduced compared to the conventional method as pictured in Fig. 15(f). Next, the v_d and v_q responses are illustrated in Fig. 15(g) and (h), respectively. The optimum bias angle applied to the CC by the FA-RPB scheme is pictured in Fig. 15(i). In which, the θ_b^m is much smoother than the experimental results due to the increased iteration count. The deviation in optimum θ_b^m under CAC+MPE and CAC+CMPE is due to the difference in rotor speed. Finally, Fig. 15(j) portrays the improvement in PF under FA-RPB-based CAC+MPE and CAC+CMPE schemes in comparison with conventional method. From the results, it is observed that, the FA-RPB schemes enable the PMVG to operate in UPF until the rotor speed reaches $0.54\omega_m^{\mathrm{r}}$ (0.8 rad/s). This indicates the validity of analytical model described in Remark 1 by using (12) and (13). Therefore, the applicability of presented FA-RPB-based CAC (Algorithm 1) for PF improvement is verified for MW class PMVGs.

F. Performance Under Parameter Variations

Next, the impact of generator parameter variations over the performance of proposed scheme has been evaluated by comparative simulation test cases. In which, the results under the conventional and proposed CMPE scheme has been availed by considering 25% and 10% perturbations, respectively, in operating parameters r_s, L_s, and compared with the ideal case results, as pictured in Fig. 16. To make the test case realistic, the parameter perturbations $\delta(r_s, L_s)$ has taken only in machine parameters and does not accounted in Algorithm 1 to identify the optimum RPB.

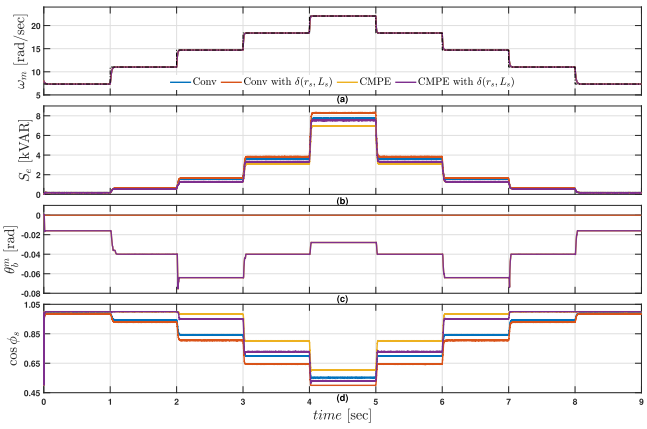

Fig. 16. Performance comparison under parameter variations. (a) Rotor speed. (b) PMVG stator reactive power. (c) Optimum RPB. (d) Power factor.

The comparative responses of rotor speed under the conventional and proposed scheme with and without $\delta(r_s, L_s)$ illustrates the effective tracking to the optimum rotor speed as in Fig. 16(a). Moreover, based on (4) and (5), the perturbations $\delta(r_s, L_s)$ influence the $[v_d\ v_q]$. As a result, the P_e, S_e, $\cos\phi_s$ differs for the ideal case and perturbation case irrespective of the incorporation of power factor improvement scheme. Comparable to the ideal case, the presented CMPE scheme achieves reduction in stator reactive power as compared to the conventional scheme with perturbations $\delta(r_s, L_s)$, as pictured in Fig. 16(b). Next, the θ_b^m responses under the test cases are drawn in Fig. 16(c). The perturbations may slightly modify the actual optimum θ_b^m, however, since the incremental step-size is taken as –0.004, the mismatch to the actual values and values used in Algorithm 1 does not cause any deviation in identified optimum θ_b^m. This is due to the fact, that the optimum θ_b^m

TABLE III
QUANTITATIVE COMPARISON OF P_e, S_e, $\cos\phi_s$ AVERAGES

Wind profile	Parameter	Conv [1]	CAC+MPE	CAC+CMPE
Step varying	$P_{e_{\text{av}}}$ [W]	2038	2007	2031
	$S_{e_{\text{av}}}$ [VAR]	2778	1724	1784
	$\cos\phi_{s_{\text{av}}}$	0.7359	0.8787	0.8737
Random varying	$P_{e_{\text{av}}}$ [W]	2286	2143	2276
	$S_{e_{\text{av}}}$ [VAR]	3169	1957	1980
	$\cos\phi_{s_{\text{av}}}$	0.7122	0.8506	0.8593

TABLE IV
COMPARATIVE EVALUATION OF VARIOUS MSES

Wind profile	Parameter	Conv [1]	PVOC	Proposed
Step varying	ω_m	0.1197	0.9564	0.1040
	$\cos\phi_s$	0.0662	0.0221	0.0197
Random varying	ω_m	1.0568	4.9987	1.0866
	$\cos\phi_s$	0.0956	0.0361	0.0390

modification resulting to the perturbation is confined within the step size –0.004. Fig. 16(d) exemplifies the PF responses of presented CMPE over the conventional scheme under ideal case and with perturbation case. From which, it is verified that, the presented scheme achieves improved power factor even under the parameter perturbations as compared to the conventional scheme.

G. Quantitative Analysis

This section comparatively analyses the generator output parameters and performance evaluation indices as follows.

1) Output Parameter Averages: The average values of operating parameters, such as PMVG output active power $P_{e_{\text{av}}}$, PMVG stator reactive power $S_{e_{\text{av}}}$, and stator PF $\cos\phi_{s_{\text{av}}}$ are comparatively evaluated for the results in Figs. 10 and 12. The average values are calculated for the entire duration of wind profiles by using the following formula [1]:

$$X_{\text{av}} = \frac{1}{T}\int_0^T x(t)dt\Big|_{X\in P_e,S_e,\cos\phi_s} \tag{21}$$

where, X_{av}, $x(t)$ is the average and instantaneous values of a specific parameter. The average values $P_{e_{\text{av}}}, S_{e_{\text{av}}}, \cos\phi_{s_{\text{av}}}$ are calculated for the results under conventional [1], CAC+MPE, and CAC+CMPE schemes and tabulated in Table III . From the results, it can be confirmed that, the FA-RPB-based CAC scheme improves the PF significantly compared with the conventional encoder-measured rotor position oriented CC. However, it has a considerable effect on MPE operation that can be compensated by the presented CMPE. Moreover, from the response plots, the proposed CAC+CMPE scheme reduces the maximum reactive power of the generator from 8420VAR to 6460VAR without a considerable effect on MPE operation. This will significantly reduce the VA ratings and cost of the converter and WTSs.

2) Comparative Performance Evaluation Indices: To signify the effectiveness of the proposed method, the mean squared error (MSE) performance index is evaluated for PMVG rotor speed and stator power factor by using (22) under traditional and proposed schemes and summarized in Table IV

$$\text{MSE} = \frac{1}{n}\sum_{\text{i=0}}^{\text{n}}(Y^* - Y)^2\Big|_{Y\in\ \omega_m,\cos\phi_s} \tag{22}$$

where n is the total number of samples taken, and Y^* and Y are the reference and measured values of the variable. The optimum rotor speed $\omega_{m_{\text{opt}}}$ is taken as the reference speed, and UPF is assumed as reference power factor to evaluate the MSE. The MSEs are evaluated for the results under random-varying and step-varying wind profiles in Figs. 12 and 14. From Table IV, traditional PVOC schemes improves the performance by minimizing the MSE in PF, however, the ω_m MSE is large due to the deviation of rotor speed from its optimum value, therefore resulting to deterioration of MPE operation. This has been resolved by the proposed CMPE by ensuring the minimum MSE. Moreover, the MSE for $[\omega_m, \cos\phi_s]$ is minimized under the proposed CMPE for both step-varying and random-varying wind profiles as compared to the traditional PVOC. Therefore, the effectiveness of the proposed scheme for power factor improvement is verified.

V. CONCLUSION

This study has presented a CMPE strategy under the CAC for PF improvement in PMVG-based WTS. To do this, an FA-RPB scheme has been proposed based on the principle of FCS-MPC. The FA-RPB is formulated as an Algorithm 1 to identify the optimum RPB through cost function optimization to improve the PMVG power factor. Next, a constrained q-axis current reference is presented to compensate the effect of RPB over the conventional MPE operation. Next, the proposed FA-RPB-based CAC for power factor improvement and CMPE is experimentally verified in 5-kW laboratory prototype of PMVG-based WTSs and the comparative results are summarized. Finally, the presented scheme's applicability to MW class PMVGs is verified through simulation. The future study will focus on developing the enhanced bias angle search strategy to achieve reduced step size with minimum iterations in FA-RPB iterative algorithm.

REFERENCES

[1] K. Palanimuthu, G. Mayilsamy, S. R. Lee, S. Y. Jung, and Y. H. Joo, "Comparative analysis of maximum power extraction and control methods between PMSG and PMVG-based wind turbine systems," *Int. J. Elect. Power Energy Syst.*, vol. 143, 2022, Art. no. 108475, doi: 10.1016/j.ijepes.2022.108475.

[2] G. Liang et al., "An enhanced distributed control architecture of multiple three-phase PMSG for improving redundancy," *IEEE Trans. Power Electron.*, vol. 38, no. 9, pp. 11338–11351, Sep. 2023.

[3] B. Kim, "Design method of a direct-drive permanent magnet vernier generator for a wind turbine system," *IEEE Trans. Ind. Appl.*, vol. 55, no. 5, pp. 4665–4675, Sep./Oct. 2019.

[4] R. Venkateswaran, A. A. Yesudhas, S. R. Lee, and Y. H. Joo, "Integral sliding mode control for extracting stable output power and regulating DC-link voltage in PMVG-based wind turbine system," *Int. J. Elect. Power Energy Syst.*, vol. 144, 2023, Art. no. 108482.

[5] Y. Gao, M. Doppelbauer, J. Ou, and R. Qu, "Design of a double-side flux modulation permanent magnet machine for servo application," *IEEE Trans. Emerg. Sel. Topics Power Electron.*, vol. 10, no. 2, pp. 1671–1682, Apr. 2022, doi: 10.1109/JESTPE.2021.3105557.

[6] H. Wang, W. Sun, D. Jiang, and R. Qu, "A MTPA and flux-weakening curve identification method based on physics-informed network without calibration," *IEEE Trans. Power Electron.*, vol. 38, no. 10, pp. 12370–12375, Oct. 2023, doi: 10.1109/TPEL.2023.3295913.

[7] Z. Ding, X. Wu, C. Chen, and X. Yuan, "Magnetic field analysis of surface-mounted permanent magnet motors based on an improved conformal mapping method," *IEEE Trans. Ind. Appl.*, vol. 59, no. 2, pp. 1689–1698, Mar./Apr. 2023, doi: 10.1109/TIA.2022.3228509.

[8] J. Zhu, Y. Zuo, H. Chen, J. Chen, and C. H. T. Lee, "Deep-investigated analytical modeling of a surface permanent magnet vernier motor," *IEEE Trans. Ind. Electron.*, vol. 69, no. 12, pp. 12336–12347, Dec. 2022, doi: 10.1109/TIE.2021.3134075.

[9] R. Venkateswaran, B. Natesan, S. R. Lee, and Y. H. Joo, "Maximum power extraction for PMVG-based WECS using q-learning MPPT algorithm with finite-time control scheme," *IEEE Trans. Sustain. Energy*, vol. 14, no. 1, pp. 516–524, Jan. 2023.

[10] F. Wu and A. M. El-Refaie, "Permanent magnet vernier machine: A review," *IET Electric Power Appl.*, vol. 13, no. 2, pp. 127–137, 2019.

[11] D. K. K. Padinharu et al., "Permanent magnet vernier machines for direct-drive offshore wind power: Benefits and challenges," *IEEE Access*, vol. 10, pp. 20652–20668, 2022.

[12] L. Deng, G. Zhou, Q. Bi, and N. Xu, "Online reactive power minimization and soft switching algorithm for triple-phase-shift modulated dual active bridge converter," *IEEE Trans. Ind. Electron.*, vol. 70, no. 3, pp. 2543–2555, Mar. 2023, doi: 10.1109/TIE.2022.3169713.

[13] K. Du, L. Xu, W. Zhao, and G. Liu, "Analysis and design of a fault-tolerant permanent magnet Vernier machine with improved power factor," *IEEE Trans. Ind. Electron.*, vol. 69, no. 5, pp. 4353–4363, May 2022, doi: 10.1109/TIE.2021.3080206.

[14] L. Xu, W. Wu, and W. Zhao, "Airgap magnetic field harmonic synergetic optimization approach for power factor improvement of PM vernier machines," *IEEE Trans. Ind. Electron.*, vol. 69, no. 12, pp. 12281–12291, Dec. 2022, doi: 10.1109/TIE.2021.3135634.

[15] Y. Zhao, D. Li, X. Ren, and R. Qu, "Investigation of permanent magnet vernier machines from armature field perspective," *IEEE Trans. Emerg. Sel. Topics Power Electron.*, vol. 10, no. 3, pp. 2934–2945, Jun. 2022, doi: 10.1109/JESTPE.2021.3058261.

[16] X. Zhao and S. Niu, "Design and optimization of a new magnetic-geared pole-changing hybrid excitation machine," *IEEE Trans. Ind. Electron.*, vol. 64, no. 12, pp. 9943–9952, Dec. 2017.

[17] M.-F. Tsai, C.-S. Tseng, and B.-Y. Lin, "Phase voltage-oriented control of a PMSG wind generator for unity power factor correction," *Energies*, vol. 13, no. 21, 2020, Art. no. 5693.

[18] S. Li, T. A. Haskew, R. P. Swatloski, and W. Gathings, "Optimal and direct-current vector control of direct-driven PMSG wind turbines," *IEEE Trans. Power Electron.*, vol. 27, no. 5, pp. 2325–2337, May 2012.

[19] L. Tong et al., "An SRF-PLL-based sensorless vector control using the predictive deadbeat algorithm for the direct-driven permanent magnet synchronous generator," *IEEE Trans. Power Electron.*, vol. 29, no. 6, pp. 2837–2849, Jun. 2014.

[20] B. Wu, Y. Lang, N. Zargari, and S. Kouro, *Power Conversion and Control of Wind Energy Systems*. Hoboken, NJ, USA: Wiley, 2011.

[21] G. Bi, N. Zhao, G. Zhang, R. Jing, G. Wang, and D. Xu, "Current vector angle adaptive adjustment based rotor position offset error suppression method for sensorless PMSM drives," *IEEE Trans. Power Electron.*, vol. 36, no. 9, pp. 10536–10547, Sep. 2021.

[22] N. A. Elsonbaty, M. A. Enany, and M. Elymany, "Concurrent unity power factor and constant mutual flux control for PMSG-WT MPPT," *Wind Eng.*, vol. 45, no. 5, pp. 1160–1174, 2021.

[23] P. M. Tlali, R.-J. Wang, S. Gerber, C. D. Botha, and M. J. Kamper, "Design and performance comparison of vernier and conventional PM synchronous wind generators," *IEEE Trans. Ind. Appl.*, vol. 56, no. 3, pp. 2570–2579, May/Jun. 2020.

[24] S.-C. Agarlita, C.-E. Coman, G.-D. Andreescu, and I. Boldea, "Stable V/f control system with controlled power factor angle for permanent magnet synchronous motor drives," *IET Electric Power Appl.*, vol. 7, no. 4, pp. 278–286, 2013.

[25] D. Ding et al., "Beatless control strategy based on impedance reshaping for PMSM drives with small DC-link capacitors," *IEEE Trans. Ind. Electron.*, vol. 71, no. 7, pp. 6829–6840, Jul. 2024, doi: 10.1109/TIE.2023.3306398.

[26] B. Nikmaram, S. A. Davari, P. Naderi, C. Garcia, and J. Rodriguez, "Sensorless simplified finite control set model predictive control of SynRM using finite position set algorithm," *IEEE Access*, vol. 9, pp. 47184–47193, 2021, doi: 10.1109/ACCESS.2021.3068085.

[27] I. Harbi et al., "Model-predictive control of multilevel inverters: Challenges, recent advances, and trends," *IEEE Trans. Power Electron.*, vol. 38, no. 9, pp. 10845–10868, Sep. 2023, doi: 10.1109/TPEL.2023.3288499.

[28] H. Xie, W. Tian, X. Gao, F. Wang, J. Rodríguez, and R. Kennel, "An ensemble regulation principle for multiobjective finite-control-set model-predictive control of induction machine drives," *IEEE Trans. Power Electron.*, vol. 38, no. 3, pp. 3069–3083, Mar. 2023, doi: 10.1109/TPEL.2022.3220289.

[29] V. Yaramasu and B. Wu, "Predictive control of a three-level boost converter and an NPC inverter for high-power PMSG-based medium voltage wind energy conversion systems," *IEEE Trans. Power Electron.*, vol. 29, no. 10, pp. 5308–5322, Oct. 2014.

[30] H. Wang, X. Wu, X. Zheng, and X. Yuan, "Model predictive current control of nine-phase open-end winding PMSMs with an online virtual vector synthesis strategy," *IEEE Trans. Ind. Electron.*, vol. 70, no. 3, pp. 2199–2208, Mar. 2023, doi: 10.1109/TIE.2022.3174241.

[31] X. Song, H. Wang, X. Ma, X. Yuan, and X. Wu, "Robust model predictive current control for a nine-phase open-end winding PMSM with high computational efficiency," *IEEE Trans. Power Electron.*, vol. 38, no. 11, pp. 13933–13943, Nov. 2023.

[32] Y. Liu, X. Liu, X. Li, H. Yuan, and Y. Xue, "Model predictive control-based dual-mode operation of an energy-stored quasi-Z-source photovoltaic power system," *IEEE Trans. Ind. Electron.*, vol. 70, no. 9, pp. 9169–9180, Sep. 2023, doi: 10.1109/TIE.2022.3215451.

[33] M. Abdelrahem, C. M. Hackl, R. Kennel, and J. Rodríguez, "Computationally efficient finite-position-set-phase-locked loop for sensorless control of PMSGs in wind turbine applications," *IEEE Trans. Power Electron.*, vol. 36, no. 3, pp. 3007–3016, Mar. 2021.

[34] J. Zhu, F. Chen, J. Chen, Y. Zuo, H. Chen, and C. H. T. Lee, "Performance improvement of surface permanent magnet vernier motor by adjusting current control angle considering magnetic saturation," in *Proc. IEEE Transp. Electrific. Conf. Expo*, 2022, pp. 61–66, doi: 10.1109/ITEC53557.2022.9813986.

[35] M. Abdelrahem, C. M. Hackl, and R. Kennel, "Finite position set-phase locked loop for sensorless control of direct-driven permanent-magnet synchronous generators," *IEEE Trans. Power Electron.*, vol. 33, no. 4, pp. 3097–3105, Apr. 2018, doi: 10.1109/TPEL.2017.2705245.

[36] Z. Yuan, S. Jia, D. Liang, X. Wang, and Y. Yang, "Research on slot-pole combination in high-power direct-drive PM vernier generator for fractional frequency transmission system," *CES Trans. Elect. Machines Syst.*, vol. 6, no. 4, pp. 445–453, Dec. 2022.

[37] G. Mayilsamy, S. R. Lee, and Y. H. Joo, "An improved model predictive control of back-to-back three-level NPC converters with virtual space vectors for high power PMSG-based wind energy conversion systems," *ISA Trans.*, vol. 143, pp. 503–524, 2023, doi: 10.1016/j.isatra.2023.09.033.

[38] K. Palanimuthu, G. Mayilsamy, S. R. Lee, S. Y. Jung, and Y. H. Joo, "Fault ride-through for PMVG-based wind turbine system using coordinated active and reactive power control strategy," *IEEE Trans. Ind. Electron.*, vol. 70, no. 6, pp. 5797–5807, Jun. 2023.

[39] G. Mayilsamy, S. R. Lee, and Y. H. Joo, "Open-switch fault diagnosis in back-to-back NPC converters of PMSG-based WTS via zero range value of phase currents," *IEEE Trans. Power Electron.*, vol. 39, no. 4, pp. 4687–4703, Apr. 2024.

Ganesh Mayilsamy received the B.E. degree in electrical and electronics engineering from the Sasurie College of Engineering, Vijayamangalam, India, in 2008, and the M.E. degree in power electronics and drives from Alagappa Chettiar Government College of Engineering and Technology, Karaikudi, India, in 2011. He is currently working toward the Ph.D. degree in electrical and electronic control engineering with the School of IT Information and Control Engineering, Kunsan National University, Gunsan, South Korea.

He was an Assistant Professor with the Department of Electrical and Electronics Engineering, P.A. College of Engineering, Pollachi, India. His research interests include power electronics drives and wind turbine control.

Byoung Chang Jeong was born in Jeonju, Korea, in 1976. He received the B.Eng. degree in electrical engineering and the Ph.D. degree in power electronics from Jeonbuk National University, Jeonju, South Korea, in 1998 and 2006, respectively.

He is currently developing PCS for ESS and other power devices at Realtech, Leimen, Germany. Since 2006, he has been in charge of developing PCS for wind power generation and for ESS at companies, such as LS Electric, Anyang-si, South Korea, and Hyosung, Seoul, South Korea. His research interests include the development of converter controllers for application to microgrids, such as the GFM inverter controller, and is also interested in controllers for stable operation of microgrids.

Seong Ryong Lee received the B.Sc. and M.Sc. degrees from Myong-Ji University, Seoul, South Korea, in 1980 and 1982, respectively, and the Ph.D. degree from Chonbuk National University, Jeonju, South Korea, in 1988, all in electrical engineering.

From 1997 to 1998, he was a Visiting Professor with the Department of Electrical and Computer Engineering, Virginia Tech., Blacksburg, VA, USA. From 2004 to 2006, he was with the Curtin University of Technology, Perth, WA, Australia. Since 1990, he has been a Professor with the School of IT Information and Control Engineering, Kunsan National University, Gunsan, South Korea. His research interests include power electronics, control, and grid-interactive renewable energy systems.

Jae Hoon Jeong received the B.S., M.S., and Ph.D. degrees in control and instrumentation engineering from Pukyong National University, Busan, South Korea, in 2015, 2017, and 2020, respectively.

In 2020, he was a Senior Researcher with the Korea Railroad Research Institute, Uiwang-si, South Korea. Since 2021, he has been an Assistant Professor with Kunsan National University, Gunsan, South Korea. His research interests include signal processing, embedded system design, sensor networks, digital control, artificial intelligence systems, and light rail transit.

Young Hoon Joo received the B.S., M.S., and Ph.D. degrees in electrical engineering from Yonsei University, Seoul, South Korea, in 1982, 1984, and 1995, respectively.

He is currently a Professor with the School of IT Information and Control Engineering, Kunsan National University, Gunsan, South Korea (1995–current). From 1986 to 1995, he was a Project Manager with Samsung Electronics Company, Seoul, South Korea. From 1998 to 1999, he was a Visiting Professor with the Department of Electrical and Computer Engineering, University of Houston, Houston, TX, USA. His research interests include control engineering, nonlinear system, intelligent control, wind energy systems, and computer vision.

Prof. Joo was the President of the Korea Institute of Intelligent Systems in 2009, the Editor-in-Chief for the *International Journal of Control, Automation, and Systems* (IJCAS, IF: 3.314) from 2014 to 2017, the Vice-President of the Institute of Control, Robot, and Control from 2016 to 2017, and the President for the Korean Institute of Electrical Engineers in 2019. He is currently the Director of the Research Center of Wind Energy Systems, Kunsan National University funded by the Korean Government (2016–current).